

Cite this: *Chem. Sci.*, 2025, **16**, 13893

All publication charges for this article have been paid for by the Royal Society of Chemistry

Received 18th April 2025
Accepted 30th June 2025

DOI: 10.1039/d5sc02835c
rsc.li/chemical-science

Introduction

The photocatalytic conversion of carbon dioxide (CO_2) into value-added fuels is a promising technology for mitigating emerging environmental crises and achieving carbon neutrality.¹ Among the diverse C_1 products (*e.g.*, CO , HCOOH , CH_3OH , CH_4 , *etc.*) derived from CO_2 reduction, methane (CH_4) is attracting significant research interest due to its high enthalpy of combustion and could replace natural gas.² Nevertheless, CH_4 production usually entails multiple proton-coupled electron transfer processes with eight electrons and reactive intermediates,³ which is kinetically sluggish relative to the competing two-electron CO_2 -to- CO process, leading to the low activity and selectivity of CH_4 formation.⁴ Therefore, to realize efficient and selective CO_2 reduction towards CH_4 products, designing photocatalysts that can manipulate the

binding strengths of C_1 intermediates and enable preferential CH_4 formation⁵ is highly desirable and imperative but remains challenging.

Generally, photocatalytic CO_2 reduction involves three vital processes: light harvesting, charge carrier separation, and CO_2 adsorption and activation.⁶ Accordingly, ideal photocatalysts should supply sufficient photogenerated charges and possess efficient carrier transfer channels to facilitate the direct transfer of electrons toward the active sites. Recently, porous conjugated polymers, including conjugated microporous polymers (CMPs)⁷⁻¹⁰ and covalent organic frameworks (COFs),¹¹⁻¹⁶ have shown great potential as catalysts or supports for CO_2 photoreduction owing to their unique advantages originating from high porosity, outstanding stability, and adjustable π -conjugated structure. Particularly, the donor-acceptor (D-A) configuration materials have attracted more attention because of the prominent photon-capture ability and the electronic pull-push effect, accelerating the splitting of photogenerated excitons.¹⁷ However, for the numerous reported D-A systems, large exciton binding energy and backward recombination of excitons still impact sufficient charge transfer to the surface,¹⁸⁻²⁰ which negatively limits their CO_2 photoreduction capability (Fig. 1a). To overcome these challenges and engineer D-A systems with enhanced photoactivity, dipole field engineering has been employed to modulate charge transport dynamics through strategic manipulation of donor and acceptor moieties.^{21,22} Generally, the high dipole moments formed by the distribution

^aCollege of Chemistry and Materials Science, Key Laboratory of Chemical Biology of Hebei Province, Hebei Research Center of the Basic Discipline of Synthetic Chemistry, Institute of Life Science and Green Development, Hebei University, Baoding, Hebei, 071002, P.R. China. E-mail: lanxingwang@hbu.edu.cn

^bKey Laboratory of Photochemical Conversion and Optoelectronic Materials & CAS-HKU Joint Laboratory on New Materials, Technical Institute of Physics and Chemistry, Chinese Academy of Sciences, Beijing 100190, P. R. China. E-mail: chenyong@mail.ipc.ac.cn

^cUniversity of Chinese Academy of Sciences, Beijing 100049, P. R. China

† Electronic supplementary information (ESI) available. See DOI: <https://doi.org/10.1039/d5sc02835c>



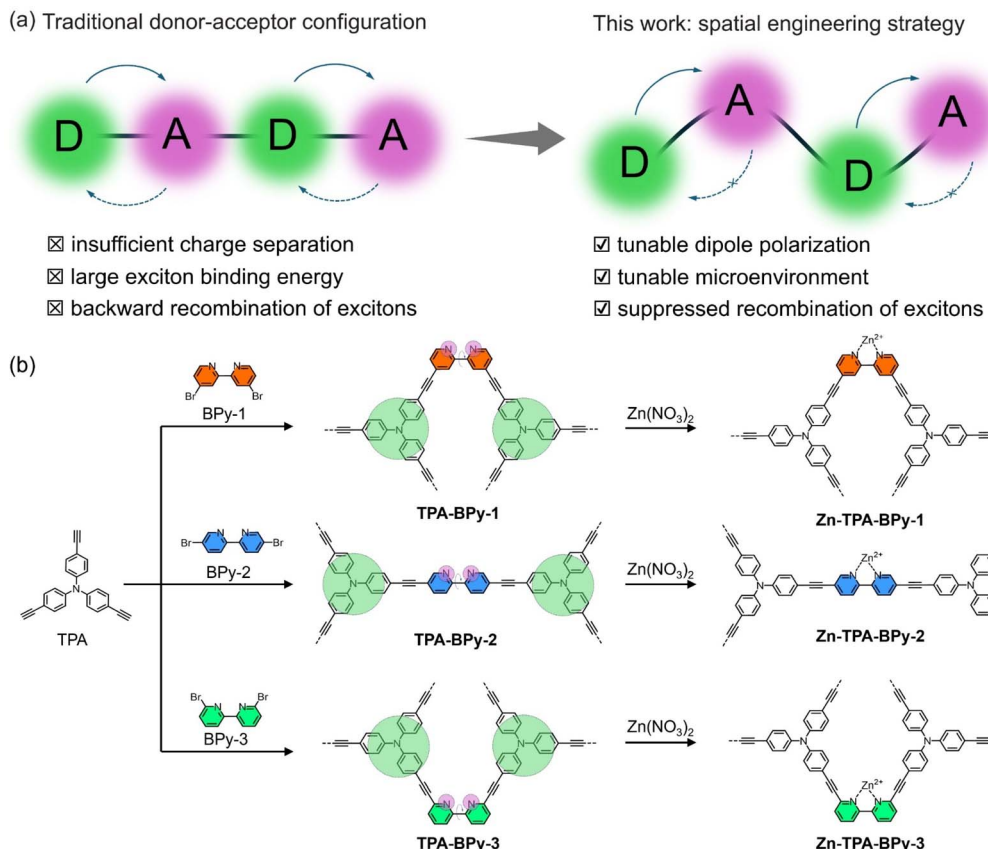


Fig. 1 (a) Scheme of the traditional donor–acceptor configuration and the design strategy for spatial engineering. (b) Synthetic routes of anchoring Zn species of TPA-BPy-1, TPA-BPy-2, and TPA-BPy-3.

of electron clouds can enhance internal polarization,²³ resulting in narrow energy gaps with red-shifted absorption and emission properties, promoting the directed charge separation during redox reactions.²⁴ Although molecular-level dipole modulation through building unit modification has achieved preliminary success, strategic spatial engineering in topological networks for directional charge transfer is rare. Particularly noteworthy is the insufficient exploration of these dipole engineering principles in CO₂ photoreduction systems. Furthermore, most organic polymeric materials suffer from the absence of catalytic active sites, leading to unsatisfactory photocatalytic performance.²⁵ To achieve high efficiency and tailored catalytic performance, various catalytic metal centers and linker molecules have been assembled into the polymer materials.^{26–28} However, the key bottleneck to effectively drive CO₂ photoreduction lies in precisely arranging the location of catalytic atoms and finely regulating the electronic state of the metal site environment.

With these considerations in mind, we propose a topological spatial engineering strategy to achieve atomic-level modulation in electronic structure tailoring and active site localization. Through regiochemical control over bipyridine substituents in modular tris(4-ethynylphenyl)amine precursors, a family of regiosomeric alkynyl-linked CMPs, namely, TPA-BPy-*n* (*n* = 1, 2, 3) were synthesized (Fig. 1b). The strategic positioning of donor

π-acceptor (D–π–A) motifs with pronounced intramolecular charge transfer (ICT) characteristics enabled systematic control over framework dipole moments, while spatial orientation precisely determines whether metal coordination occurs inside or outside the channels. Based on these, the atomically dispersed Zn sites were incorporated into bipyridine units of TPA-BPy-*n* for photocatalytic CO₂ reduction. Photocatalytic evaluations revealed that single Zn sites located outside the channels of TPA-BPy-1, possessing the longest dipole moment, exhibited higher kinetic activity, CH₄ and CO production-rates at 753.2 and 233.9 μmol g⁻¹ h⁻¹, respectively, and the CH₄-product selectivity at 89.7%. Combined with the experimental and theoretical results, we demonstrated that the effects of intramolecular dipole polarization and microenvironment can effectively modulate catalytic performances. This work highlights that the topology-driven dipole programming strategy can modulate the electronic structure of active sites to promote photocatalytic CO₂ reduction.

Results and discussion

Synthesis and characterization

The TPA-BPy-*n* (*n* = 1, 2, 3) substrates bearing D–π–A units were synthesized by the Sonogashira–Hagihara reaction between tris(4-ethynylphenyl)amine (TPA) and bipyridine skeletons with



bromine atoms as the active sites (see ESI† for details). In this process, the bipyridine units as bidentate ligands orient in different crosslinking directions by varying the substituent position of bipyridines, and alkynes are connected to monomers as bridging units and arranged in bonding directions to form a periodic topology. The TPA-BPy-1 and TPA-BPy-3 enforce a V-shaped geometry, promoting twisted polymer chains and non-interpenetrated networks. The TPA-BPy-3 with linear geometry facilitates extended conjugation and rigid, ordered frameworks. Prior to characterizations, the electronic distribution and hole–electron separation efficiency of TPA-BPy-*n* was studied using density functional theory (DFT) calculations for the simplified structure models. These polymer fragments display typical donor–acceptor configurations. The highest occupied molecular orbital (HOMO) and lowest unoccupied molecular orbital (LUMO) are mainly localized on the TPA (electron acceptor) and bipyridine (electron acceptor) unit of the frameworks (Fig. S1†), implying that TPA-BPy-*n* has a strong ICT interaction from donor to acceptor moiety through the π -bridge to reduce the overlap of the hole and electron distributions.^{29,30} Furthermore, electrostatic potential (ESP) distributions of the three model structures show that spatial structural engineering causes the increase of dipole moment and internal spontaneous polarization, resulting in an uneven spatial charge distribution and the formation of localized dipoles within the molecule.³¹ The dipole moment magnitudes of TPA-BPy-1, TPA-BPy-2, and TPA-BPy-3 are 10.4384 D, 3.9958 D, and 1.0286 D, respectively (Fig. 2a). Particularly, the dipole moment of TPA-BPy-1 is significantly higher than that of TPA-BPy-2 and TPA-BPy-3. This

elevated molecular dipole moment facilitates efficient charge transfer within the molecule. Theoretical analyses of frontier orbital distributions and molecular dipole moments suggest that the spatial engineering in TPA-BPy-*n* induces localized polarization, enhancing exciton dissociation and the generation of photogenerated carriers under visible light.^{32–34}

Further insights into the electron–hole distribution in the excited state of TPA-BPy-1, TPA-BPy-2, and TPA-BPy-3 fragments were obtained by time-dependent-density functional theory (TD-DFT) calculation and electron–hole excitation analysis with *Multiwfn* software.^{35–37} As shown in Fig. S2–S4,† the degree of electron–hole separation of TPA-BPy-1 is remarkably higher than that of TPA-BPy-2 and TPA-BPy-3, where the positive and negative charges are mainly located in the TPA and bipyridine units, respectively. Moreover, some key parameters were calculated to investigate the subtle changes in these fragments during the excitation process (Table S1†). As expected, TPA-BPy-1 has the largest *D* value (1.901 Å) and lowest Sr index (0.752) in the first singlet excited states (S_1), indicating a better hole–electron separation performance of TPA-BPy-1 compared with TPA-BPy-2 and TPA-BPy-3 (Fig. 2b). The electron density difference between the first excited and ground states further supports this superior hole–electron separation efficiency of TPA-BPy-1. Temperature-dependent photoluminescence (PL) spectroscopy was systematically employed to investigate the charge transfer dynamics in the TPA-BPy-*n* series. As illustrated in Fig. 2c–f, a distinct temperature-dependent enhancement of integrated PL intensity is observed for all TPA-BPy-*n*, following a characteristic pattern of thermally activated nonradiative

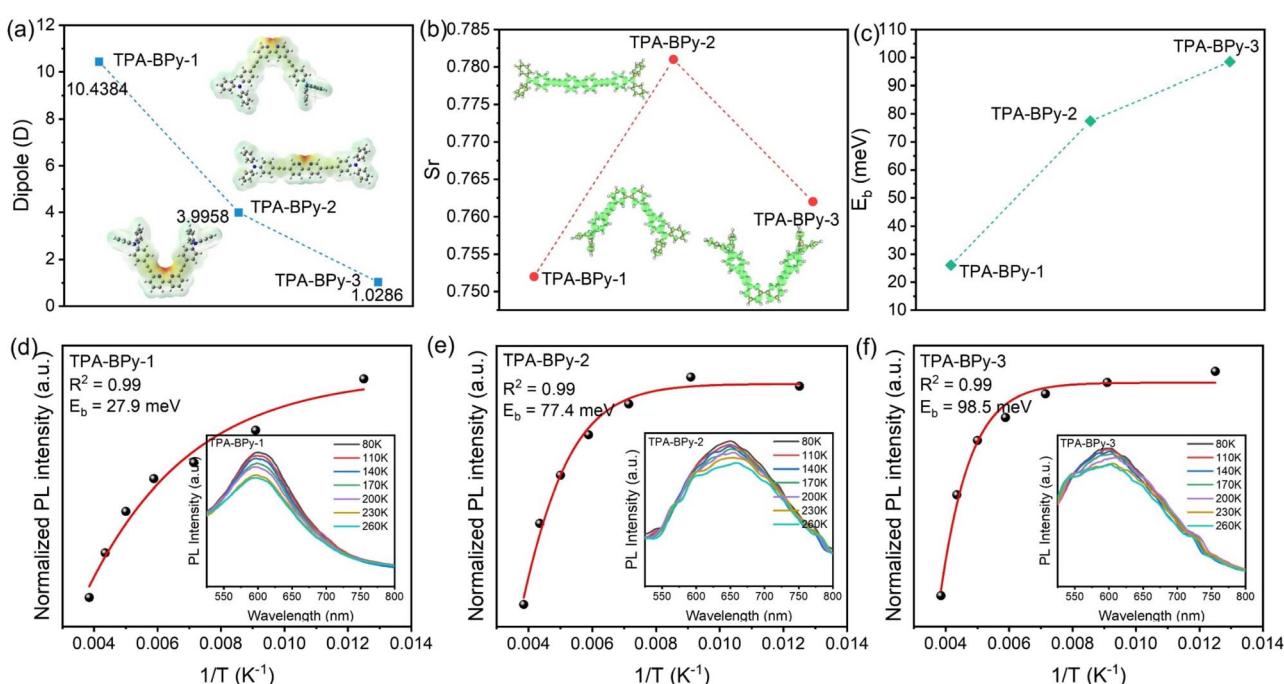


Fig. 2 (a) Dipole moments magnitudes and ESP distribution maps of TPA-BPy-1, TPA-BPy-2, and TPA-BPy-3 fragments. (b) The overlap between the electron and hole distributions of three fragments in the S_1 excited state. The Sr is the hole–electron overlap indicator. (c) Experimental exciton binding energy of TPA-BPy-1, TPA-BPy-2, and TPA-BPy-3 by the Arrhenius equation. (d–f) Temperature-dependent PL spectra and integrated PL emission intensity as a function of temperature from 80 to 260 K.



recombination processes.³⁸ This temperature-dependent behavior is quantitatively analyzed through Arrhenius formalism using the equation: $I(T) = I_0/(1 + A \exp(-E_b/k_B T))$, where I_0 is the intensity at 0 K, k_B is the Boltzmann constant, and E_b is the exciton binding energy.³⁹ Through nonlinear least-squares fitting of the experimental data, the exciton binding energies are determined to be 27.9, 77.4, and 98.5 meV for TPA-BPy-1, TPA-BPy-2, and TPA-BPy-3, respectively. This progressive increase in E_b values along the series (TPA-BPy-1 < TPA-BPy-2 < TPA-BPy-3) establishes a clear correlation between molecular structure and exciton stability. The relatively lower binding energy observed in TPA-BPy-1 suggests enhanced exciton dissociation efficiency compared to its higher counterparts, potentially originating from reduced coulombic interactions.⁴⁰ Theoretical and experimental results collectively show that spatial structural engineering significantly enhances hole-

electron separation efficiency in these polymers. The high dipole polarization is beneficial for boosting exciton dissociation efficiency, which plays a vital role in determining their photocatalytic activity.

The defined chemical structures of TPA-BPy-*n* were systematically confirmed by Fourier transform infrared spectroscopy (FT-IR) and solid-state ¹³C cross-polarization/magic angle spinning nuclear magnetic resonance (CP/MAS NMR) analyses. FT-IR spectra of three CMPs (Fig. 3a) exhibit distinct stretching vibrations at the stretching vibration peak of C≡C at ~ 2184 cm⁻¹, and the C=C of benzenes at ~ 1500 cm⁻¹ can be observed (Fig. 3a). Notably, the C=N stretching frequency of pyridine moieties in TPA-BPy-1 appears at ~ 1580 cm⁻¹ in TPA-BPy-1, displaying obvious shifts compared to TPA-BPy-2 and TPA-BPy-3 due to electron-withdrawing conjugation effects between pyridinic nitrogen and adjacent alkyne groups in the

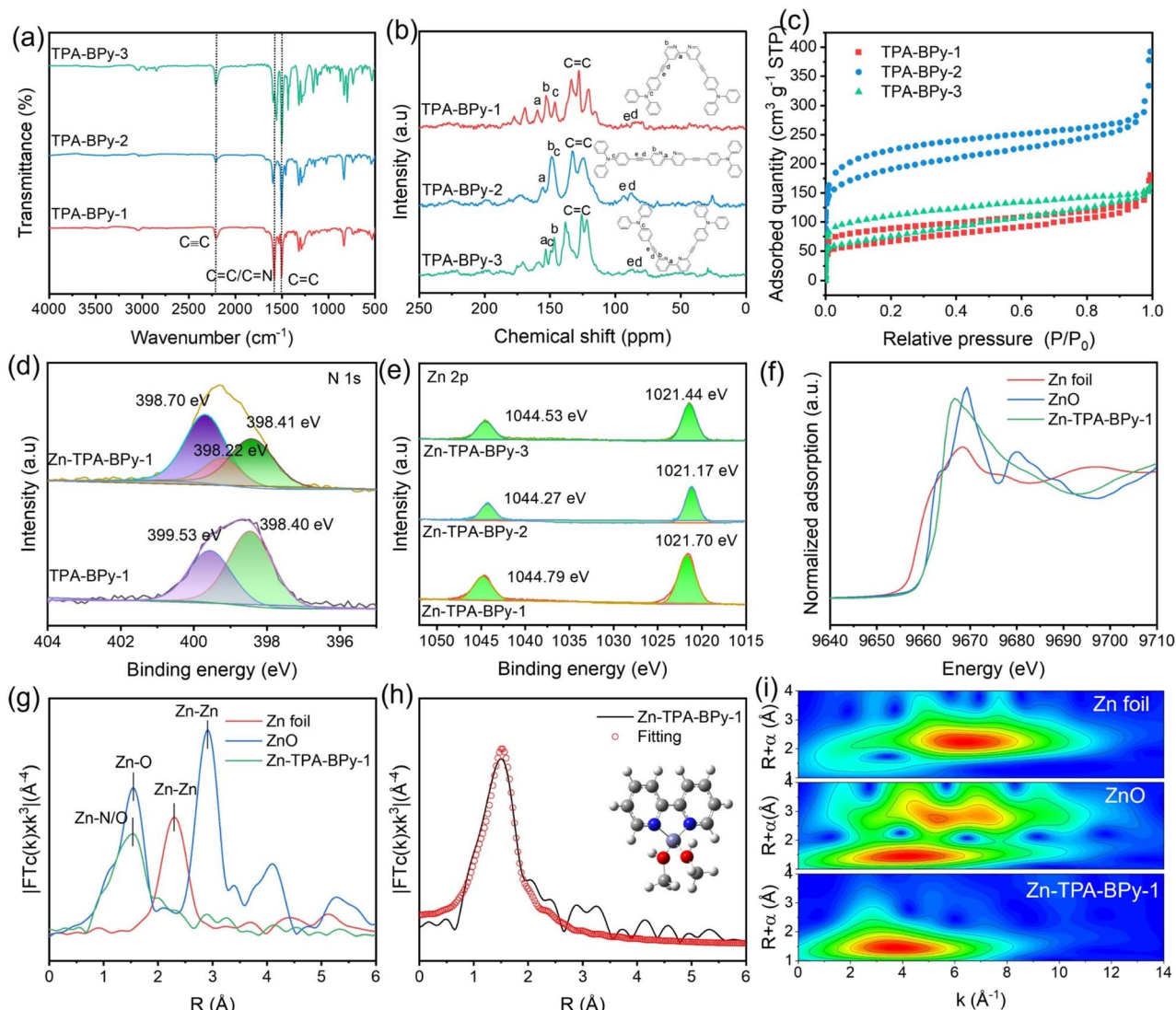


Fig. 3 (a) FT-IR spectra, (b) solid-state ¹³C NMR spectra, and (c) N₂ sorption isotherms of TPA-BPy-*n*. (d) High-resolution N 1s XPS spectra of Zn-TPA-BPy-1 and TPA-BPy-1. (e) Zn 2p XPS spectra of Zn-TPA-BPy-*n*. (f) Zn K-edge XANES and (g) Fourier-transformed EXAFS spectra of Zn foil, ZnO, and Zn-TPA-BPy-1. (h) Zn K-edge XANE fitting analyses for Zn-TPA-BPy-1 in *R* space. (i) The wavelet transforms of EXAFS spectra for Zn-TPA-BPy-1 and reference samples.



regioisomeric topology. Meanwhile, the C≡C-H and C-Br stretching vibration signals cannot be identified in the FT-IR spectra of CMPs (Fig. S5–S7†), indicating the successful polymerization of monomers. The expected peaks for the carbon atoms in the C≡C bond at ~87 and ~90 ppm can be observed in the ¹³C NMR spectra of CMPs (Fig. 3b). The carbon atoms near pyridine N correspond to the peak at about ~150 ppm, and the peaks of aromatic carbons are found at 116–134 ppm. The PXRD analysis suggests the amorphous nature with a broad hump at $2\theta = 21.2^\circ$ due to the interlayer π - π interaction of the phenyl ring (Fig. S8†). In addition, thermogravimetric analysis of TPA-BPy-*n* shows their decomposition temperature above 420 °C (Fig. S9†), demonstrating their good thermal stability. The permanent porosities of TPA-BPy-*n* were investigated by N₂ adsorption–desorption measurement at 77 K (Fig. 3c). All the sorption isotherms of TPA-BPy-*n* can be identified as the typical type-IV sorption curves with steep gas uptake in the low relative pressure range and distinct hysteresis loop, indicative of microporous and mesoporous characteristics. The Brunauer–Emmett–Teller (BET) specific surface areas of TPA-BPy-1, TPA-BPy-2, and TPA-BPy-3 are calculated to be 237.8, 423.2, and 222.8 m² g⁻¹, respectively. Additionally, the pore size distribution curves exhibit that TPA-BPy-1 and TPA-BPy-3 with distorted V-shaped geometry induces tighter packing and balances micro/mesoporosity, yielding intermediate pore size. In contrast, TPA-BPy-2 with uniform geometry and channels can obviously enhance the surface area with main microporosity (Fig. S10†). Scanning electron microscopy (SEM) and transmission electron microscopy (TEM) display that TPA-BPy-*n* possesses a similar particle-stacked morphology with particle sizes in the range of 200–400 nm (Fig. S11†).

Subsequently, to study the influence of the bipyridine ligand's spatial location, Zn species (Zn(NO₃)₂) were integrated into dipyridine units through post-modification using methanol solvent (see details in ESI†). The resulting Zn–N bonds restrict C–C bond rotation, enhancing molecular rigidity. Inductively coupled plasma-mass spectrometry (ICP-OES) detection reveals that the Zn contents of Zn-TPA-BPy-1, Zn-TPA-BPy-2, and Zn-TPA-BPy-3 are 1.49, 1.47, and 1.55 wt%, respectively, where only partially bipyridine units are coordinated with Zn²⁺ in the skeletons. FT-IR and PXRD characterizations all reveal that the morphology and structure of TPA-BPy-*n* are retained after incorporating Zn species (Fig. S12 and S13†). Following, take Zn-TPA-BPy-1 for example, N₂ adsorption–desorption measurement was conducted to investigate the change of porosity and morphology. The N₂ sorption curve of Zn-TPA-BPy-1 still presents the type IV isotherms with a BET surface area of 202.30 m² g⁻¹ (Fig. S14†). The slight decrease in specific surface area can be caused by the space occupations by introducing Zn species. TEM images in Fig. S15† reveal that after incorporating Zn²⁺ ions, the original morphology of TPA-BPy-1 is not changed. Energy dispersive spectroscopy (EDS) elemental mappings of Zn-TPA-BPy-1 distinctly portray the homogeneous spatial distribution of C, N, and Zn, revealing that Zn species are uniformly dispersed across the surface of TPA-BPy-1. X-ray photoelectron spectroscopy (XPS) was conducted to ascertain their chemical compositions and electronic

states. The XPS survey spectra confirm the presence of C, N, and target Zn elements in Zn-TPA-BPy-*n* (Fig. S16a†). The high-resolution C 1s spectra are deconvoluted into two main peaks at 284.80 and 285.63 eV, corresponding to C=C/C≡C and C=N bonds, respectively (Fig. S16b†). The high-resolution N 1s spectra of TPA-BPy-1 can be resolved into C–N (398.40 eV) of TPA and C=N (399.53 eV) of bipyridine units.⁴¹ Compared to the TPA-BPy-1, the C=N signal (398.70 eV) of bipyridine units occur obvious shift in the Zn-TPA-BPy-1, besides, a new Zn–N peak can be deconvoluted in the 398.22 eV,⁴² corresponding to the coordination between Zn and bipyridine, as shown in Fig. 3d and S16c.† The Zn 2p spectra exhibit two characteristic Zn 2p_{3/2} peaks (1021.17 eV) and Zn 2p_{1/2} peaks (1044.27 eV) in Zn-TPA-BPy-1 (Fig. 3e), respectively, unambiguously verifying the +2 oxidation state of Zn center.⁴³ Moreover, the Zn 2p_{3/2} spectra for Zn-TPA-BPy-1 show distinct binding energy shifts relative to Zn-TPA-BPy-2 and Zn-TPA-BPy-3. The obvious shifts are ascribed to the different coordination environments within the molecular frameworks, which increases the effective nuclear charge experienced by Zn centers through ligand-mediated polarization effects. The Zn K-edge X-ray absorption near edge structure (XANES) spectrum for Zn-TPA-BPy-1 (Fig. 3f) is close to the ZnO, confirming the existence of Zn²⁺ species.⁴⁴ The Zn K-edge extended X-ray absorption fine structure (EXAFS) spectra demonstrate the Zn–N/O coordination with a distance of 1.98 ± 0.02 Å (Zn–N) and 2.09 ± 0.02 Å (Zn–O)⁴⁵ (Fig. 3g). No Zn–Zn bond is observed, implying the isolated Zn atoms anchor on the support. The coordination numbers of the Zn atom are investigated by fitting analysis of EXAFS spectra (Fig. 3h and Table S2†), from which Zn exhibits a coordination number close to 4 (Zn–N₂O₂). Specifically, single-atom Zn center is possibly coordinated with bidentate dipyridine and two methanol molecules. The wavelet transforms (WT) analysis of Zn-TPA-BPy-1 further shows an intensity maximum close to ZnO rather than Zn foils (Fig. 3i), suggesting the maintenance of Zn–N/O structure in Zn-TPA-BPy-1.

Photocatalytic CO₂ reduction performance of catalysts

The photocatalytic CO₂ reduction performance of these samples was investigated under simulated solar illumination conditions in a pure-water system with triethanolamine (TEOA) as electron donor and [Ru(bpy)₃]Cl₂·6H₂O (abbreviated as Ru) as photosensitizer. To verify the role of Zn species in the catalytic reaction, pristine TPA-BPy-*n* was tested. The results show that TPA-BPy-*n* mainly implements CO₂ reduction to CO with minimal selectivity towards CH₄ (Fig. 4a). In contrast, the structural incorporation of Zn sites induces a product selectivity shift from predominant CO to CH₄ evolution, while demonstrating superior catalytic activity compared to transition metal counterparts (e.g., Co, Ni, Cu) (Fig. S17†). Specifically, in terms of the CO₂-to-CH₄ conversion, Zn-TPA-BPy-1 achieves a CH₄ evolution rate of 753.2 $\mu\text{mol g}^{-1} \text{h}^{-1}$, nearly 58.9-fold enhancement of TPA-BPy-1, while the selectivity also incredibly increases from 61.1% to 89.7% (electron selectivity). As observed from the time-yield plots, the rate of product evolution increases linearly during the catalytic process (Fig. 4b). The CH₄ production rate is quite



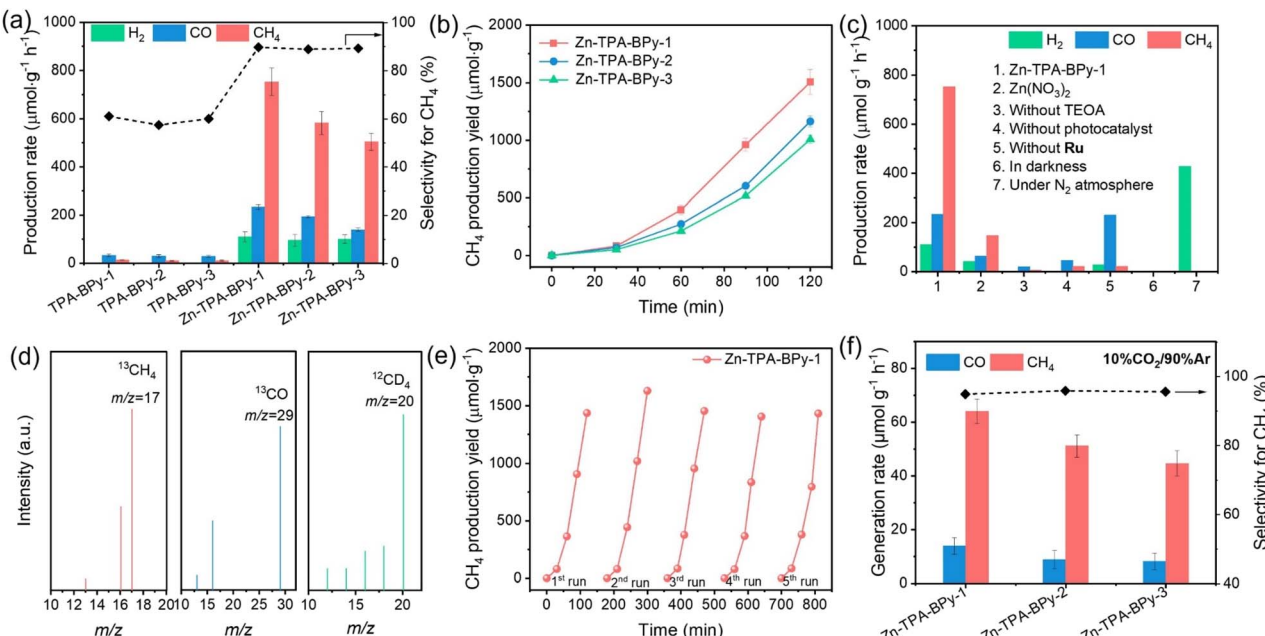


Fig. 4 (a) Photocatalytic CO_2 activities of pristine TPA-BPy-*n* and Zn-TPA-BPy-*n*. (b) Time courses of CH_4 evolution by photocatalytic CO_2 reduction using Zn-TPA-BPy-*n* photocatalysts for 2 h, with evacuation every 0.5 h. (c) The photocatalytic performance of Zn-TPA-BPy-1 under different conditions. (d) Mass spectra for CO_2 reduction of Zn-TPA-BPy-1 using $^{13}\text{CO}_2$ as the reacting gas or D_2O as solvent. (e) Cycling experiments of Zn-TPA-BPy-*n*. (f) Photocatalytic activities of Zn-TPA-BPy-*n* under diluted CO_2 (10% CO_2 and 90% Ar) atmosphere.

competitive with many reported photocatalysts (Table S3†). Impressively, Zn-TPA-BPy-1 exhibits superior catalytic activity compared to Zn-TPA-BPy-2 and Zn-TPA-BPy-3, which indicates the critical role of metal coordination geometry in modulating active site electronic states. Notably, compared to Zn-TPA-BPy-2 and Zn-TPA-BPy-3, Zn-TPA-BPy-1 still presents higher activity from time-yield plots. Furthermore, the measured apparent quantum yield (AQY) of CH_4 evolution for Zn-TPA-BPy-1 can achieve the maximum value of 3.45% at 450 nm (Fig. S18†).

Control experiments were conducted to understand the reaction progress, and the results are shown in Fig. 4c. While $\text{Zn}(\text{NO}_3)_2$ demonstrated catalytic activity for CO_2 reduction to CH_4 ($146.9 \mu\text{mol g}^{-1} \text{h}^{-1}$), its performance was significantly lower than Zn-TPA-BPy-1, confirming that the TPA-BPy-1 framework is essential for enabling Zn species to selectively drive CH_4 production. Only extremely small amounts of carbon products could be detected without adding photocatalyst and TEOA, where the carbon products possibly origin from the catalysis of Ru for CO_2 photoreduction. These results confirm that photocatalyst and TEOA are indispensable in this system. However, in the absence of Ru, Zn-TPA-BPy-1 exhibits predominant CO evolution with a rate of $230.27 \mu\text{mol g}^{-1} \text{h}^{-1}$, accompanied by only trace CH_4 generation. This marked product distribution disparity highlights the critical role of Ru and photocatalysts in synergistically mediating energy transfer to active sites, thereby facilitating proton-coupled electron transfer during intermediate stabilization in the CO_2 reduction pathway.⁴⁶ Furthermore, no detectable products are observed in the dark or N_2 feeding gas condition, which affirms that the formed CH_4 and CO are indeed derived from CO_2

photoreduction. The isotope labeling experiment was conducted to verify further the origin of carbon products (Fig. 4d). The typical mass spectrum signals of $^{13}\text{CH}_4$ ($m/z = 17$) and ^{13}CO ($m/z = 29$) can be observed after pumping $^{13}\text{CO}_2$ as the only carbon source, verifying that the detected carbon products are indeed generated from the CO_2 photoreduction. Meanwhile, the appearance of the CD_4 ($m/z = 20$) signal using D_2O instead of H_2O suggests that H_2O is the source of hydrogen in CH_4 rather than TEOA in the CO_2 -to- CH_4 conversion. Additionally, residual Pd and Cu from Sonogashira-Hagihara coupling are unavoidable and can potentially contribute to CO_2 reduction as additional metal cocatalysts. ICP-OES analysis confirmed similar residual Pd and Cu levels across all catalysts (Table S4†), yet their activities differed substantially, especially Zn-TPA-BPy-1 exhibited notably higher activity. This indicates that performance differences likely do not originate from residual Pd or Cu. Furthermore, a control catalyst (Zn-TPA-BPy-1-M) was prepared using fivefold higher $\text{Pd}(\text{PPh}_3)_4$ and CuI , yielding significantly elevated Pd (2.30 wt%) and Cu (0.75 wt%) content. Notably, the production rates of CH_4 and CO decreased rather than increasing as expected, whereas H_2 production was enhanced (Fig. S19†). These experiments indicate that the residual Pd and Cu do not significantly participate in the photocatalytic CO_2 reduction in this work, but their existence is beneficial for H_2 evolution, resulting in the decreased selectivity. Besides, cycling tests were also carried out on the Zn-TPA-BPy-*n* to reveal their stability. As displayed in Fig. 4e, the activity of CO_2 photoreduction to CH_4 presents a negligible decline after five cycles for Zn-TPA-BPy-1. It is worth noting that Zn-TPA-BPy-1 presents a higher CH_4 evolution rate observed from the time-

yield plots than Zn-TPA-BPy-2 and Zn-TPA-BPy-3 during the five cycles (Fig. S20†). Moreover, the SEM and FT-IR of Zn-TPA-BPy-1 show that the morphology and structure of the catalyst remained unchanged (Fig. S21 and S22†), illustrating the excellent durability of our catalysts.

Inspired by the excellent photocatalytic activity of Zn-TPA-BPy-*n* in a pure CO₂ atmosphere, diluted CO₂ (10% CO₂ and 90% Ar) was then used to further investigate their reduction activities (Fig. 4f). Encouragingly, under visible light irradiation, Zn-TPA-BPy-1 still shows a higher CH₄ evolution rate of 64.05 μmol g⁻¹ h⁻¹ with a selectivity of 94.9% by using diluted CO₂ as the source than Zn-TPA-BPy-2 and Zn-TPA-BPy-3. The remarkable activity of Zn-TPA-BPy-1 for CH₄ production should be attributed to the synergistic contribution of TPA-BPy-1 and Zn sites in enriching diluted CO₂.

Exploration of intrinsic catalytic activity enhancement

To unveil the underlying reasons for the high CO₂ reduction activity of Zn-TPA-BPy-1, the mechanistic insights toward the light-harvesting capacity and charge transfer behavior were analyzed. UV-vis diffuse reflectance spectra (DRS) of Zn-TPA-BPy-1 show a higher light absorption intensity and a remarkable red shift of the absorption edge with an expanded absorption tail compared to those of Zn-TPA-BPy-2 and Zn-TPA-BPy-3 (Fig. 5a), indicating the improved optical properties and enhanced light harvesting ability due to distinct configuration. Accordingly, the band gaps (E_g) of these samples are calculated to be 2.08, 2.15, and 2.38 eV for Zn-TPA-BPy-1, Zn-TPA-BPy-2, and Zn-TPA-BPy-3, respectively, from the corresponding Tauc

plots. Zn-TPA-BPy-1 exhibits a narrower bandgap, which facilitates the transition of photogenerated electrons.⁴⁷ Mott-Schottky measurements were then carried out to determine the flat band potentials (E_{FB}) (Fig. S23†). The positive slopes of the M-S plots indicate that Zn-TPA-BPy-*n* are typical n-type semiconductors, and the E_{FB} of Zn-TPA-BPy-1, Zn-TPA-BPy-2, and Zn-TPA-BPy-3 can be determined to be -1.18, -1.16, and -1.07 V vs. NHE (normal hydrogen electrode, pH = 7), that is, -1.38, -1.36, and -1.27 V (vs. Ag/AgCl), respectively. In general, conduction band potential (E_{CB}) is approximately equal to the E_{FB} for n-type semiconductors,⁴⁸ thus valence band potential (E_{VB}) of Zn-TPA-BPy-*n* series can be calculated to be 0.90, 0.99, and 1.31 V vs. NHE, respectively, by the equation $E_{VB} = E_{CB} + E_g$. Band alignment in Fig. 5b reveal that all Zn-TPA-BPy-*n* catalysts exhibit more positive E_{CB} potentials compared to Ru photosensitizer, creating a substantial thermodynamic driving force for directional electron transfer from photoexcited Ru to Zn catalytic centers. This charge transfer mechanism effectively suppresses electron-hole recombination while maintaining strong redox capacities.⁴⁹ Crucially, E_{CB} of Zn-TPA-BPy-*n* has more negative theoretical potentials for CO₂ reduction to CO and CH₄.⁵⁰ Such favorable band energetics not only ensure thermodynamic feasibility but also enable kinetically favorable multi-electron transfer processes for CH₄ production.

To elucidate the photoinduced charge carrier dynamics, we conducted systematic photophysical characterization through steady-state photoluminescence (PL) and time-resolved transient photoluminescence (TRPL) spectroscopy. As shown in Fig. 5c, Zn-TPA-BPy-1 displays marked PL quenching compared with Zn-TPA-BPy-3 and Zn-TPA-BPy-2, indicating that the carrier

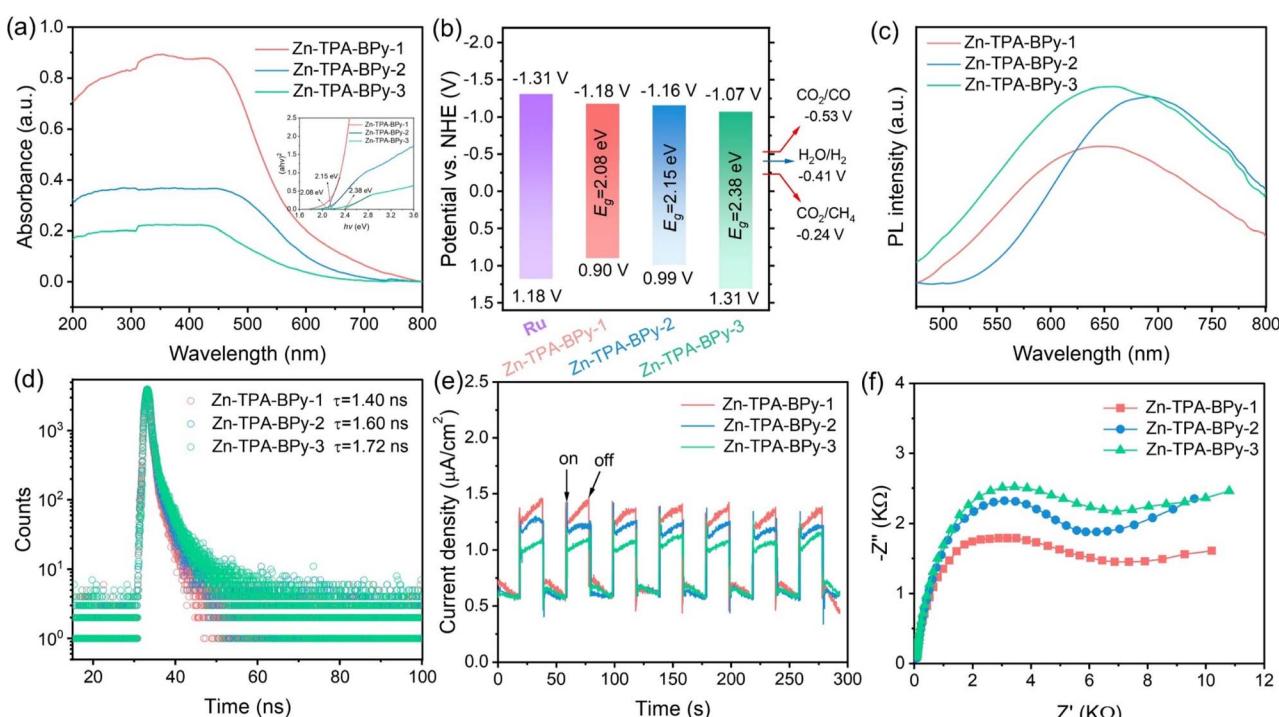


Fig. 5 (a) Solid-state UV-vis DRS spectra (inset: Tauc plots), (b) band structure alignment, (c) PL spectra, (d) TR-PL plots, (e) transient photocurrent responses and (f) EIS curves of the as-prepared Zn-TPA-BPy-1, Zn-TPA-BPy-2, and Zn-TPA-BPy-3 samples.



recombination of Zn-TPA-BPy-1 is greatly suppressed, which represents the higher separation efficiency of photogenerated charges. The TRPL curve of Zn-TPA-BPy-1 in Fig. 5d exhibits that the average carrier lifetime of Zn-TPA-BPy-1 (1.40 ns) is shortened compared to Zn-TPA-BPy-2 (1.60 ns) and Zn-TPA-BPy-3 (1.72 ns), indicating that the photogenerated charges in Zn-TPA-BPy-1 transport much faster. It can be thus speculated that the localized asymmetric charge polarization in TPA-BPy-1 facilitates ultrafast photoinduced charge transfer and charge separation from donor to acceptor, and then rapid electron injection into Zn sites.^{51–53} The transient photocurrent curves and electrochemical impedance spectroscopy (EIS) spectra provided additional corroboration to this observation. Owing to the synergetic effects of enhanced light absorption and inhibited exciton recombination, Zn-TPA-BPy-1 displays higher photocurrent density and smaller semicircle in the Nyquist plots compared to Zn-TPA-BPy-2 and Zn-TPA-BPy-3 (Fig. 5e and f), demonstrating its more photogenerated free charge carriers and efficient interface transfer resistance for improved charge transfer efficiency. Additionally, lifetime, photoconductivity, and resistivity of parent TPA-BPy-1, TPA-BPy-2, and TPA-BPy-3 follows a similar trend; however, their efficiency was significantly improved upon Zn incorporation (Fig. S24–S26†). Moreover, TD-DFT hole-electron analysis reveals electron/hole distribution in bipyridine units and Zn sites. Zn-TPA-BPy-*n* exhibits lower Sr and higher *D* values than TPA-BPy-*n* (Fig. S27 and Table S5†), indicating Zn sites can also facilitate charge transfer and charge separation. It can be thus concluded that the regioisomer-dependent π -topology significantly influences polarity and optoelectronic properties. Crucially, asymmetric structures with high dipole polarization enable effective charge transport and separation, directing charges to bipyridine units (electron collection center) to activate the Zn site for CO₂ reduction.

Underlying mechanism of photocatalytic CO₂ reduction

To unveil the actual reaction mechanism, the CO₂ adsorption capacities of Zn-TPA-BPy-*n* were first evaluated. The CO₂ adsorption isotherms in Fig. 6a illustrate that all Zn-TPA-BPy-*n* possesses high CO₂ adsorption capacities. These results suggest that TPA-BPy-*n* can enrich local CO₂ molecules on the catalyst surface, and the high CO₂ physisorption is beneficial for promoting the CO₂ reduction process. Notably, Zn-TPA-BPy-1 exhibits a higher CO₂ uptake than Zn-TPA-BPy-2 and Zn-TPA-BPy-3. This physical adsorption is likely to be enhanced by the upgraded spatial configuration of TPA-BPy-1, which improves its capability to activate CO₂ molecules. The *in situ* diffuse reflectance infrared Fourier transformation spectroscopy (DRIFTS) measurements were conducted on Zn-TPA-BPy-1 with light irradiation to probe the key reaction intermediates (Fig. 6b). When CO₂ molecules are injected into the reactor under a dark environment, several peaks assigned to bidentate carbonate (b-CO₃²⁻, 1575 and 1673 cm⁻¹), monotonic carbonate (m-CO₃²⁻, 1310 cm⁻¹), and bicarbonate (HCO₃⁻, 1431 cm⁻¹) species^{54,55} are observed in the collected spectra, indicating that CO₂ molecules are adsorbed and activated on

the surface. Upon illumination, these peak intensities are enhanced, while new absorption peaks of *COOH (1224, 1343, and 1532 cm⁻¹)^{56,57} and *CO absorption intermediates (1917 cm⁻¹)⁵⁸ gradually appear. More importantly, the pivotal intermediate *CHO (1088 cm⁻¹) for the formation of CH₄ is observed,⁵⁹ which can be ascribed to the proton from the vapor reacted with *CO intermediate. Moreover, the characteristic peaks of *CH₃O (974, 1040, and 1749 cm⁻¹) and *CH₃ (2891 and 2982 cm⁻¹) also appear, representing key intermediates for the generation of CH₄. This reaction pathway leads to photocatalytic CO₂-to-CH₄ reaction pathways of the Zn-TPA-BPy-1 sample under illumination.

DFT calculations were then conducted on Zn-TPA-BPy-*n* to further verify the possible photocatalytic CO₂-to-CH₄ pathway. According to the free energy diagrams (Fig. 6c and d), the formations of *CO₂ on Zn-TPA-BPy-*n* are exothermic processes, indicating the high efficiency of CO₂ activation due to the synergistic effect between the TPA-BPy-*n* and Zn site. Despite lower adsorption energy, Zn-TPA-BPy-3 requires 0.41 eV energy expenditure for the *COOH formation step, higher than Zn-TPA-BPy-1 and Zn-TPA-BPy-2. Note that the C–O bond cleavage in *COOH to form *CO is a highly endergonic, rate-limiting step. Zn-TPA-BPy-1 exhibits a lower energy barrier for *CO formation ($\Delta G = 1.48$ eV) than Zn-TPA-BPy-2 (1.53 eV) and Zn-TPA-BPy-3 (1.62 eV). By balancing *CO₂ adsorption energy with *COOH and *CO formation energies, TPA-BPy-1 lowers reaction barriers, strengthens metal-site bonding, and enhances photocatalytic CO₂ reduction activity. Moreover, *CO desorption and hydrogenation to *CHO, the key intermediate to form CH₄, are exothermic spontaneously. However, the *CHO intermediate is validated to form preferentially during the *CO transformation process, thereby diminishing the selectivity of CO and realizing the selective CH₄ evolution. Additionally, the formation of CH₃OH* intermediates can be another rate-limiting step for hydrogenation processes, where Zn-TPA-BPy-3 exhibits a higher energy barrier compared to Zn-TPA-BPy-1 and Zn-TPA-BPy-2, impeding *CH₃ formation from CH₃OH* *via* dehydration. These DFT calculations suggest that the whole process of CO₂ photoreduction into CH₄ reaction on Zn-TPA-BPy-1 is more favorable in thermodynamics. Thus, it can be believed that the high polarity and outside-channel active sites are beneficial for modulating the reaction energy barrier of *COOH and *CO intermediates to facilitate the selectivity-determining protonation of *CO to *CHO intermediates, thereby regulating the reaction activity during the CO₂ reduction process.

Based on the above results, a reasonable mechanism for CO₂ photoreduction on Zn-TPA-BPy-*n* was proposed, as illustrated in Fig. 6e. Under visible light irradiation, photoexcited electrons are generated on the Ru photosensitizer, which then transfer to TPA-BPy-*n* and flow to the Zn sites to participate in the reduction of CO₂ molecules adsorbed on the surface of catalysts, during which TEOA acted as a sacrificial agent to complete the Ru cycle.⁶⁰ We then carried out PL spectroscopy to verify the photogenerated electron transfer process. As shown in Fig. S28,† adding Zn-TPA-BPy-1 quenches the emission of Ru ($\lambda_{\text{em}} = \text{ca. } 620 \text{ nm}$), while no significant change occurs when



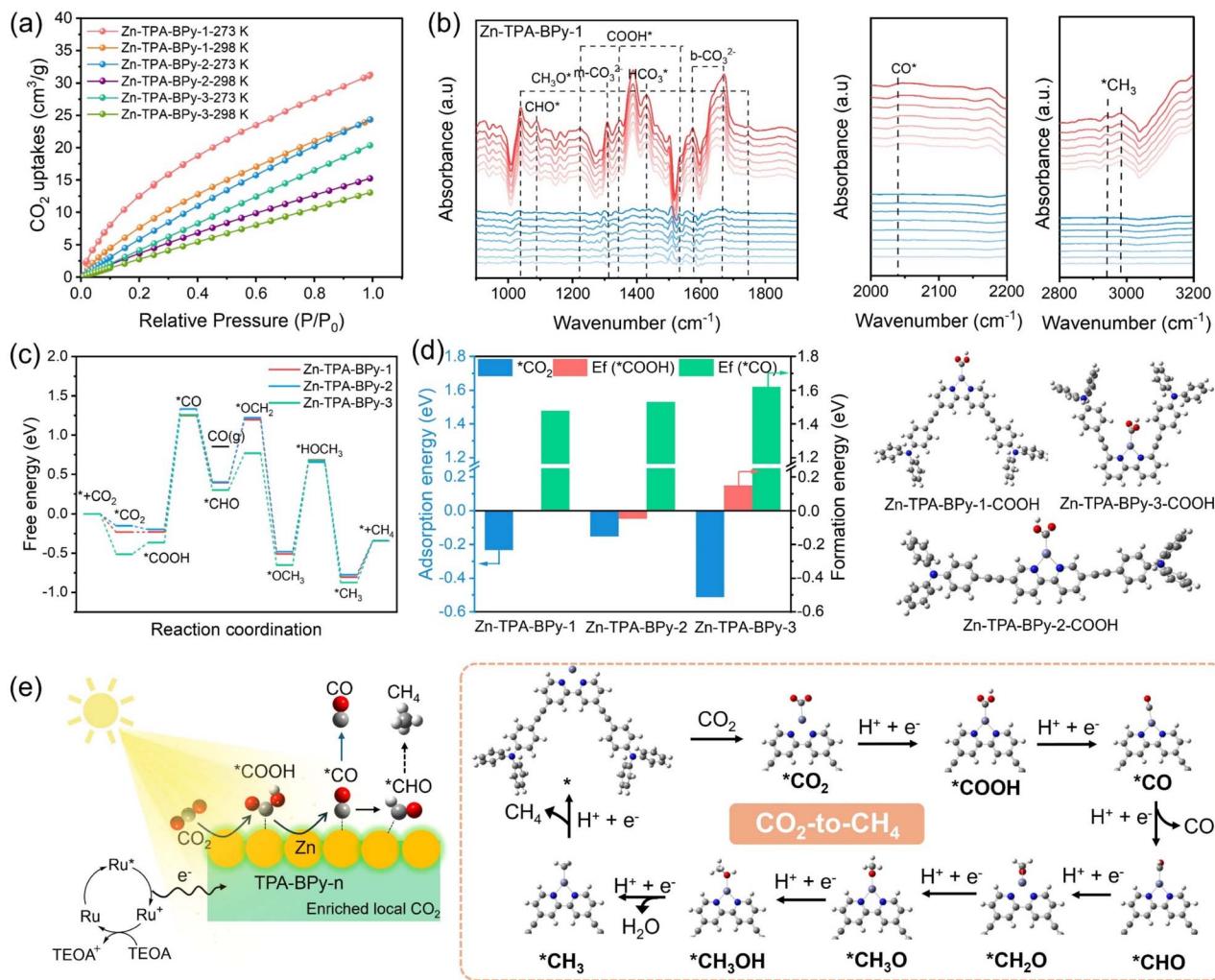


Fig. 6 (a) CO₂ adsorption isotherms of Zn-TPA-BPy-1, Zn-TPA-BPy-2, and Zn-TPA-BPy-3 samples. (b) *In situ* DRIFTS spectra of Zn-TPA-BPy-1 sample showing the reaction pathways of photocatalytic CO₂-to-CH₄ process in the dark (blue lines) and light irradiation (red lines). (c) Gibbs free energy (ΔG , eV) profiles of photoreduction of CO₂ over Zn-TPA-BPy-*n*. (d) The adsorption energy of *CO₂ and formation energy of *COOH and *CO on Zn-TPA-BPy-*n*. (e) Schematic illustration showing possible reaction pathway for photocatalytic CO₂ reduction on the Zn-TPA-BPy-*n*.

adding TEOA, which provides an evidence that the catalyst effectively takes up the photogenerated electrons from Ru to achieve the eight-electron CH₄ pathway by continuous electron transport.⁶¹ The excellent activity and selectivity of Zn-TPA-BPy-1 for photocatalytic CO₂ reduction to CH₄ primarily stem from its enhanced charge transfer ability, lower activation barriers for the generation of the key intermediates *COOH and *CO, and the thermodynamically favorable formation of *CHO. These factors are closely related to the unique spatial configuration, endowing Zn atoms with a higher activity.

Conclusions

In summary, three Zn-TPA-BPy-*n* (*n* = 1, 2, 3) catalysts are constructed by varying the arrangement in bonding directions of bipyridine substituents to form spatially distinct periodic topologies for photocatalytic CO₂ reduction. Remarkably high catalytic activities are exhibited by the designed systems, particularly Zn-TPA-BPy-1, which achieves a CH₄ production

rate of 753.2 $\mu\text{mol g}^{-1} \text{h}^{-1}$ with 89.7% selectivity. Experimental and theoretical results reveal that TPA-BPy-1 with high dipole moment and sites anchored outside pore walls can facilitate dipole-induced internal polarization and mass transport, enabling the Zn active site for efficient CO₂ conversion. Detailed mechanistic studies demonstrate that the synergistic effect of the Zn sites and TPA-BPy-1 reduces the energy barrier for *COOH and *CO intermediates, and thermodynamically favors the formation of *CHO intermediates, thus boosting selective photoreduction of CO₂ to CH₄. This work provides new insight into designing efficient organic photocatalysts containing more abundant metals toward highly selective CH₄ production and a reasonable mechanism for CO₂ reduction.

Data availability

Further details of the experimental procedure, figures, tables, and calculations are available in the ESI.†



Author contributions

X. L. and Y. C. supervised the project. J. W. and L. C. synthesized the catalysts. J. W. and L. C. carried out photocatalytic experiments. J. W., L. C., and H. X. characterized the materials. T. Z. carried out synchrotron radiation. X. L. conducted DFT calculations. X. L. and Y. C. co-wrote the manuscript. All authors discussed the results and contributed to the preparation of the manuscript.

Conflicts of interest

The authors declare no conflict of interest.

Acknowledgements

This work was financially supported by the National Natural Science Foundation of China (22421005 and 21908038), Natural Science Foundation of Hebei Province (B2024201017 and B2023201108), Science Research Project of Hebei Education Department (BJK2022045), Hebei Province Innovation Capability Enhancement Plan Project (22567632H), and Youth Top Talent Project of Hebei University. The authors also acknowledge the High-Performance Computing Center of Hebei University.

Notes and references

- 1 S. Fang, M. Rahaman, J. Bharti, E. Reisner, M. Robert, G. A. Ozin and Y. H. Hu, Photocatalytic CO₂ reduction, *Nat. Rev. Methods Primers*, 2023, **3**, 61.
- 2 U. Ulmer, T. Dingle, P. N. Duchesne, R. H. Morris, A. Tavasoli, T. Wood and G. A. Ozin, Fundamentals and applications of photocatalytic CO₂ methanation, *Nat. Commun.*, 2019, **10**, 3169.
- 3 Y. Wang, E. Chen and J. Tang, Insight on Reaction Pathways of Photocatalytic CO₂ Conversion, *ACS Catal.*, 2022, **12**, 7300–7316.
- 4 S. Si, H. Shou, Y. Mao, X. Bao, G. Zhai, K. Song, Z. Wang, P. Wang, Y. Liu, Z. Zheng, Y. Dai, L. Song, B. Huang and H. Cheng, Low-Coordination Single Au Atoms on Ultrathin ZnIn₂S₄ Nanosheets for Selective Photocatalytic CO₂ Reduction towards CH₄, *Angew. Chem., Int. Ed.*, 2022, **61**, e202209446.
- 5 J. Li, H. Huang, W. Xue, K. Sun, X. Song, C. Wu, L. Nie, Y. Li, C. Liu, Y. Pan, H.-L. Jiang, D. Mei and C. Zhong, Self-adaptive dual-metal-site pairs in metal-organic frameworks for selective CO₂ photoreduction to CH₄, *Nat. Catal.*, 2021, **4**, 719–729.
- 6 C. Feng, Z. P. Wu, K. W. Huang, J. Ye and H. Zhang, Surface modification of 2D photocatalysts for solar energy conversion, *Adv. Mater.*, 2022, **34**, 2200180.
- 7 F. Meng, J. Wang, M. Chen, Z. Wang, G. Bai and X. Lan, Extending the π -conjugated system in conjugated microporous polymers to modulate excitonic effects for metal-free selective CO₂ photoreduction to CH₄, *ACS Catal.*, 2023, **13**, 12142–12152.

- 8 M. G. Mohamed, C. C. Chen, M. Ibrahim, A. Osama Mousa, M. H. Elsayed, Y. Ye and S. W. Kuo, Tetraphenylanthraquinone and Dihydroxybenzene-Tethered Conjugated Microporous Polymer for Enhanced CO₂ Uptake and Supercapacitive Energy Storage, *JACS Au*, 2024, **4**, 3593–3605.
- 9 F. A. Rahimi, S. Dey, P. Verma and T. K. Maji, Photocatalytic CO₂ reduction based on a Re (I)-integrated conjugated microporous polymer: role of a sacrificial electron donor in product selectivity and efficiency, *ACS Catal.*, 2023, **13**, 5969–5978.
- 10 Z. Tang, S. Xu, N. Yin, Y. Yang, Q. Deng, J. Shen, X. Zhang, T. Wang, H. He, X. Lin, Y. Zhou and Z. Zou, Reaction Site Designation by Intramolecular Electric Field in Tröger's-Base-Derived Conjugated Microporous Polymer for Near-Unity Selectivity of CO₂ Photoconversion, *Adv. Mater.*, 2023, **35**, 2210693.
- 11 W. Lin, F. Lin, J. Lin, Z. Xiao, D. Yuan and Y. Wang, Efficient photocatalytic CO₂ reduction in ellagic acid-based covalent organic frameworks, *J. Am. Chem. Soc.*, 2024, **146**, 16229–16236.
- 12 X. Lan, H. Li, Y. Liu, Y. Zhang, T. Zhang and Y. Chen, Covalent Organic Framework with Donor¹-Acceptor-Donor² Motifs Regulating Local Charge of Intercalated Single Cobalt Sites for Photocatalytic CO₂ Reduction to Syngas, *Angew. Chem., Int. Ed.*, 2024, **63**, e202407092.
- 13 S. Yang, R. Sa, H. Zhong, H. Lv, D. Yuan and R. Wang, Microenvironments enabled by covalent organic framework linkages for modulating active metal species in photocatalytic CO₂ reduction, *Adv. Funct. Mater.*, 2022, **32**, 2110694.
- 14 Y. Z. Cheng, W. Ji, P. Y. Hao, X. H. Qi, X. Wu, X. M. Dou, X. Y. Bian, D. Jiang, F. T. Li, X. F. Liu, D. H. Yang, X. Ding and B. H. Han, A Fully Conjugated Covalent Organic Framework with Oxidative and Reductive Sites for Photocatalytic Carbon Dioxide Reduction with Water, *Angew. Chem., Int. Ed.*, 2023, **62**, e202308523.
- 15 Q. Xu, J. Han, F. Tian, X. Zhao, J. Rong, J. Zhang, P. She, J. S. Qin and H. Rao, Synergistic Bifunctional Covalent Organic Framework for Efficient Photocatalytic CO₂ Reduction and Water Oxidation, *J. Am. Chem. Soc.*, 2025, **147**, 10587–10597.
- 16 M. Yu, W. Chen, Q. Lin, L. Li, Z. Liu, J. Bi and Y. Yu, Electrostatic Confinement-Induced Excited Charge Transfer in Ionic Covalent Organic Framework Promoting CO₂ Reduction, *Angew. Chem., Int. Ed.*, 2025, **64**, e202418422.
- 17 C. Yang, S. Wan, B. Zhu, J. Yu and S. Cao, Calcination-regulated microstructures of donor-acceptor polymers towards enhanced and stable photocatalytic H₂O₂ production in pure water, *Angew. Chem., Int. Ed.*, 2022, **61**, e202208438.
- 18 L. Wang, L. Liu, Y. Li, Y. Xu, W. Nie, Z. Cheng, Q. Zhou, L. Wang and Z. Fan, Molecular-level regulation strategies toward efficient charge separation in donor-acceptor type conjugated polymers for boosted energy-related photocatalysis, *Adv. Energy Mater.*, 2024, **14**, 2303346.



19 Z. Lin, S. Dai, S. Yao, Q. C. Lin, M. Fu, L. H. Chung, B. Han and J. He, Diacetylene-bridged covalent organic framework as crystalline graphdiyne analogue for photocatalytic hydrogen evolution, *Chem. Sci.*, 2025, **16**, 1948–1956.

20 F. Yu, Z. Zhu, S. Wang, J. Wang, Z. Xu, F. Song, Z. Dong and Z. Zhang, Novel donor-acceptor-acceptor ternary conjugated microporous polymers with boosting forward charge separation and suppressing backward charge recombination for photocatalytic reduction of uranium (VI), *Appl. Catal., B*, 2022, **301**, 120819.

21 H. Yang, R. Zhao, J. Wang, X. Yin, Z. Lu and L. Hou, Local electron donor defects induce dipole polarization boosting on covalent organic frameworks to promote photocatalysis, *ACS Mater. Lett.*, 2023, **5**, 2877–2886.

22 R. Shen, X. Li, C. Qin, P. Zhang and X. Li, Efficient Photocatalytic Hydrogen Evolution by Modulating Excitonic Effects in Ni-Intercalated Covalent Organic Frameworks, *Adv. Energy Mater.*, 2023, **13**, 2203695.

23 Z. Li, Y. Zhou, Y. Zhou, K. Wang, Y. Yun, S. Chen, W. Jiao, L. Chen, B. Zou and M. Zhu, Dipole field in nitrogen-enriched carbon nitride with external forces to boost the artificial photosynthesis of hydrogen peroxide, *Nat. Commun.*, 2023, **14**, 5742.

24 W. Zeng, Y. Dong, X. Ye, Z. Zhang, T. Zhang, X. Guan and L. Guo, Crystalline carbon nitride with in-plane built-in electric field accelerates carrier separation for excellent photocatalytic hydrogen evolution, *Chin. Chem. Lett.*, 2024, **35**, 109252.

25 B. B. Rath, S. Krause and B. V. Lotsch, Active site engineering in reticular covalent organic frameworks for photocatalytic CO₂ reduction, *Adv. Funct. Mater.*, 2024, **34**, 2309060.

26 D. T. Nguyen and T. O. Do, Comprehensive Review for an Efficient Charge Transfer in Single Atomic Site Catalyst/Organic Polymers toward Photocatalytic CO₂ Reduction, *Adv. Mater. Interfaces*, 2023, **10**, 2201413.

27 A. F. Saber, A. M. Elewa, H. H. Chou and A. F. EL-Mahdy, Donor-acceptor carbazole-based conjugated microporous polymers as photocatalysts for visible-light-driven H₂ and O₂ evolution from water splitting, *Appl. Catal., B*, 2022, **316**, 121624.

28 B. Huang, X. Tang, Y. Hong, L. Li, T. Hu, K. Yuan and Y. Chen, Electron-donors-acceptors interaction enhancing electrocatalytic activity of metal-organic polymers for oxygen reduction, *Angew. Chem., Int. Ed.*, 2023, **62**, e202306667.

29 N. Liu, S. Xie, Y. Huang, J. Lu, H. Shi, S. Xu, G. Zhang and X. Chen, Dual-Acceptor Engineering in Pyrene-Based Covalent Organic Frameworks for Boosting Photocatalytic Hydrogen Evolution, *Adv. Energy Mater.*, 2024, **14**, 2402395.

30 Y. Qi, J. Zhang, Y. Kong, Y. Zhao, S. Chen, D. Li, W. Liu, Y. Chen, T. Xie, J. Cui, C. Li, K. Domen and F. Zhang, Unraveling of cocatalysts photodeposited selectively on facets of BiVO₄ to boost solar water splitting, *Nat. Commun.*, 2022, **13**, 484.

31 M. Liu, C. X. Cui, S. Yang, X. Yang, X. Li, J. He, Q. Xu and G. Zeng, Elaborate Modulating Binding Strength of Intermediates via Three-component Covalent Organic Frameworks for CO₂ Reduction Reaction, *Angew. Chem., Int. Ed.*, 2024, **136**, e202401750.

32 L. Hao, R. Shen, S. Chen, W. Bi, L. Wang, G. Liang, P. Zhang and X. Li, Boosting exciton dissociation and charge separation in pyrene-based linear conjugated polymers for efficient photocatalytic hydrogen production, *J. Mater. Chem. A*, 2022, **10**, 24064.

33 W. Li, B. Han, Y. Liu, J. Xu, H. He, G. Wang, J. Li, Y. Zhai, X. Zhu and Y. Zhu, Unsymmetric Protonation Driven Highly Efficient H₂O₂ Photosynthesis in Supramolecular Photocatalysts via One-Step Two-Electron Oxygen Reduction, *Angew. Chem., Int. Ed.*, 2025, **64**, e202421356.

34 C. Zhu, M. Yang, B. Jiang, L. Lu, Q. Fang, Y. Zheng, S. Song, B. Chen and Y. Shen, Insights into excitonic behavior in single-atom covalent organic frameworks for efficient photo-Fenton-like pollutant degradation, *Nat. Commun.*, 2025, **16**, 790.

35 C. Ru, X. Nie, Z. A. Lan, Z. Pan, W. Xing, S. Wang, J. C. Yu, Y. Hou and X. Wang, Regulation of Exciton Effects in Functionalized Conjugated Polymers by B-N Lewis Pairs for Visible-Light Photocatalysis, *Angew. Chem., Int. Ed.*, 2025, **64**, e202417712.

36 T. Lu and F. Chen, Multiwfn: A multifunctional wavefunction analyzer, *J. Comput. Chem.*, 2012, **33**, 580–592.

37 T. Lu, A comprehensive electron wavefunction analysis toolbox for chemists, Multiwfn, *J. Chem. Phys.*, 2024, **161**, 082503.

38 Z. Wang, C. Zhang, H. Wang, Y. Xiong, X. Yang, Y. Shi and A. Rogach, Two-Step Oxidation Synthesis of Sulfur with a Red Aggregation-Induced Emission, *Angew. Chem., Int. Ed.*, 2020, **59**, 9997–10002.

39 Y. Chen, Y. Cheng, Y. Liu, Y. Wang, Y. Qu, D. Jiang, Z. Qin and Y. Yuan, Achieving long-lived shallow trapping states in carbon nitride through the n-π* electronic transition for enhanced photocatalytic hydrogen generation, *Appl. Catal., B*, 2024, **342**, 123453.

40 X. Deng, N. Gao and L. Bai, Bromine Atoms Decorated Pyrene-based Covalent Organic Frameworks for Accelerated Photocatalytic H₂ Production, *Small*, 2024, **20**, 2311927.

41 W. Liu, P. Wang, J. Chen, X. Gao, H. Che, B. Liu and Y. Ao, Unraveling the mechanism on ultrahigh efficiency photocatalytic H₂O₂ generation for dual-heteroatom incorporated polymeric carbon nitride, *Adv. Funct. Mater.*, 2022, **32**, 2205119.

42 J. Wang, H. Li, S. Liu, Y. Hu, J. Zhang, M. Xia, Y. Hou, J. Tse, J. Zhang and Y. Zhao, Turning on Zn 4s Electrons in a N₂-Zn-B₂ Configuration to Stimulate Remarkable ORR Performance, *Angew. Chem., Int. Ed.*, 2021, **60**, 181–185.

43 W. Wang, R. Liu, J. Zhang, T. Kong, L. Wang, X. Yu, X. Ji, Q. Liu, R. Long, Z. Lu and Y. Xiong, Building Asymmetric Zn–N₃ Bridge between 2D Photocatalyst and Co-catalyst for Directed Charge Transfer toward Efficient H₂O₂ Synthesis, *Angew. Chem., Int. Ed.*, 2025, **64**, e202415800.

44 Y. L. Jia, Z. Q. Xue, J. Yang, Q. L. Liu, J. H. Xian, Y. C. Zhong, Y. M. Sun, X. X. Zhang, Q. H. Liu, D. X. Yao and G. Q. Li, Tailoring the Electronic Structure of an Atomically Dispersed Zinc Electrocatalyst: Coordination Environment



Regulation for High Selectivity Oxygen Reduction, *Angew. Chem., Int. Ed.*, 2022, **61**, e202110838.

45 Y. Yang, H. Y. Zhang, Y. Wang, L. H. Shao, L. Fang, H. Dong, M. Lu, L. Z. Dong, Y. Q. Lan and F. M. Zhang, Integrating Enrichment, Reduction, and Oxidation Sites in One System for Artificial Photosynthetic Diluted CO₂ Reduction, *Adv. Mater.*, 2023, **35**, 2304170.

46 C. Ning, J. Yang, S. Bai, G. Chen, G. Liu, T. Shen, L. Zheng, S. M. Xu, X. Kong, B. Liu, Y. Zhao and Y. F. Song, An Efficient Intercalation Supramolecular Structure for Photocatalytic CO₂ Reduction to Ethylene Under Visible Light, *Adv. Funct. Mater.*, 2023, **34**, 2300365.

47 T. Huang, J. Kou, H. Yuan, H. Guo, K. Yuan, H. Li, F. Wang and Z. Dong, Linker Modulation of Covalent Organic Frameworks at Atomic Level for Enhanced and Selective Photocatalytic Oxidation of Thioether, *Adv. Funct. Mater.*, 2025, **35**, 2413943.

48 L. Zhang, Z. Chen, X. X. Li, X. Wang, Q. Gu, X. Wang, C. S. Lee, Y. Q. Lan and Q. Zhang, A Covalent Organic Nanoribbon: Preparation, Single-Crystal Structure with Chinese Luban Lock Configuration, and Photocatalytic Behavior, *Angew. Chem., Int. Ed.*, 2024, **63**, e202411018.

49 C. Xu, S. Yu, M. Zhang, X. Zhan, S. Jiang, S. Wang, G. Liu, J. Ren, X. Sun, Y. Wang, H. Q. Peng, B. Liu, W. Zhang and Y. F. Song, Synergistic Engineering of Electron-Enriched Nickel Sites for Highly Efficient Photocatalytic CO₂ Reduction to C₂H₆, *Adv. Funct. Mater.*, 2025, **35**, 2414893.

50 Y. Shi, G. Zhan, H. Li, X. Wang, X. Liu, L. Shi, K. Wei, C. Ling, Z. Li, H. Wang, C. Mao, X. Liu and L. Zhang, Simultaneous Manipulation of Bulk Excitons and Surface Defects for Ultrastable and Highly Selective CO₂ Photoreduction, *Adv. Mater.*, 2021, **33**, 2100143.

51 J. Wu, K. Li, B. Zhou, R. Li, S. Yan, J. Liu, H. Shi, C. Song and X. Guo, Bottom-Up Strategy to Enhance Long-Range Order of Poly(Heptazine Imide) Nanorods for Efficient Photocatalytic CO₂ Methanation, *Angew. Chem., Int. Ed.*, 2025, **64**, e202421263.

52 L. Qin, D. Sun, D. Ma, Z. Wang, Y. Liu, Q. Li, F. Song, K. Wu, L. Gan, T. Zhou and J. Zhang, Decoupling Interlayer Interactions Boosts Charge Separation in Covalent Organic Frameworks for High-Efficiency Photocatalytic CO₂ Reduction, *Adv. Mater.*, 2025, **37**, 2504205.

53 J. Li, M. Du, Z. Wu, X. Zhang, W. Xue, H. Huang and C. Zhong, Engineering Single-Atom Sites with the Irving-Williams Series for the Simultaneous Co-photocatalytic CO₂ Reduction and CH₃CHO Oxidation, *Angew. Chem., Int. Ed.*, 2024, **63**, e202407975.

54 B. Zhang, H. Li, Y. Kang, K. Yang, H. Liu, Y. Zhao and S. Qiao, Metal-Ion-Coordinated Microenvironments in Covalent Organic Frameworks for Enhanced Photocatalytic CO₂ Reduction, *Adv. Funct. Mater.*, 2025, **35**, 2416958.

55 X. Zu, Y. Zhao, X. Li, R. Chen, W. Shao, Z. Wang, J. Hu, J. Zhu, Y. Pan, Y. Sun and Y. Xie, Ultrastable and Efficient Visible-light-driven CO₂ Reduction Triggered by Regenerative Oxygen-Vacancies in Bi₂O₂CO₃ Nanosheets, *Angew. Chem., Int. Ed.*, 2021, **60**, 13840–13846.

56 T. Wang, L. Chen, C. Chen, M. Huang, Y. Huang, S. Liu and B. Li, Engineering Catalytic Interfaces in Cu^{δ+}/CeO₂-TiO₂ Photocatalysts for Synergistically Boosting CO₂ Reduction to Ethylene, *ACS Nano*, 2022, **16**, 2306–2318.

57 R. Xu, D. Si, S. Zhao, Q. Wu, X. Wang, T. Liu, H. Zhao, R. Cao and Y. Huang, Tandem Photocatalysis of CO₂ to C₂H₄ via a Synergistic Rhenium-(I) Bipyridine/Copper-Porphyrinic Triazine Framework, *J. Am. Chem. Soc.*, 2023, **145**, 8261–8270.

58 P. Liu, Z. Huang, X. Gao, X. Hong, J. Zhu, G. Wang, Y. Wu, J. Zeng and X. Zheng, Synergy between Palladium Single Atoms and Nanoparticles via Hydrogen Spillover for Enhancing CO₂ Photoreduction to CH₄, *Adv. Mater.*, 2022, **34**, 2200057.

59 X. Yang, L. Ren, Z. Chen, H. Li and Y. Yuan, Constructing an Active Sulfur-Vacancy-Rich Surface for Selective *CH₃-CH₃ Coupling in CO₂-to-C₂H₆ Conversion With 92% Selectivity, *Adv. Mater.*, 2025, **37**, 2412299.

60 F. Meng, R. Zhang, H. Xu, L. Shen, H. Yang, Q. Meng and X. Lan, Engineering copper single sites in conjugated microporous polymers to enhance selective photocatalytic CO₂ methanation, *Chem. Eng. J.*, 2025, **511**, 162017.

61 J. Liu, B. Han, X. Liu, S. Liang, Y. Fu, J. He, L. H. Chung, Y. Lin, Y. Wei, S. Wang, T. Ma and Z. Yang, Tailoring d-Band Center of Single-Atom Nickel Sites for Boosted Photocatalytic Reduction of Diluted CO₂ from Flue Gas, *Angew. Chem., Int. Ed.*, 2025, **64**, e202417435.

